Relative Contributions of Mean-State Shifts and ENSO-Driven Variability to Precipitation Changes in a Warming Climate*

CÉLINE J. W. BONFILS, BENJAMIN D. SANTER, THOMAS J. PHILLIPS, AND KATE MARVEL+

Program for Climate Model Diagnosis and Intercomparison, Lawrence Livermore National Laboratory, Livermore, California

L. RUBY LEUNG

Pacific Northwest National Laboratory, Richland, Washington

CHARLES DOUTRIAUX

Program for Climate Model Diagnosis and Intercomparison, Lawrence Livermore National Laboratory, Livermore, California

ANTONIETTA CAPOTONDI

University of Colorado, and NOAA/Earth System Research Laboratory, Boulder, Colorado

(Manuscript received 12 May 2015, in final form 2 October 2015)

ABSTRACT

El Niño–Southern Oscillation (ENSO) is an important driver of regional hydroclimate variability through far-reaching teleconnections. This study uses simulations performed with coupled general circulation models (CGCMs) to investigate how regional precipitation in the twenty-first century may be affected by changes in both ENSO-driven precipitation variability and slowly evolving mean rainfall. First, a dominant, time-invariant pattern of canonical ENSO variability (cENSO) is identified in observed SST data. Next, the fidelity with which 33 state-of-the-art CGCMs represent the spatial structure and temporal variability of this pattern (as well as its associated precipitation responses) is evaluated in simulations of twentieth-century climate change. Possible changes in both the temporal variability of this pattern and its associated precipitation teleconnections are investigated in twenty-first-century climate projections. Models with better representation of the observed structure of the cENSO pattern produce winter rainfall teleconnection patterns that are in better accord with twentieth-century observations and more stationary during the twenty-first century. Finally, the model-predicted twenty-first-century rainfall response to cENSO is decomposed into the sum of three terms: 1) the twenty-first-century change in the mean state of precipitation, 2) the historical precipitation response to the cENSO pattern, and 3) a future enhancement in the rainfall response to cENSO, which amplifies rainfall extremes. By examining the three terms jointly, this conceptual framework allows the identification of regions likely to experience future rainfall anomalies that are without precedent in the current climate.

Denotes Open Access content.

* Supplemental information related to this paper is available at the Journals Online website: http://dx.doi.org/10.1175/JCLI-D-15-0341.s1.

+ Current affiliation: NASA Goddard Institute for Space Studies, and Department of Applied Physics and Applied Mathematics, Columbia University, New York, New York.

Corresponding author address: Céline J. W. Bonfils, Lawrence Livermore National Laboratory, Program for Climate Model Diagnosis and Intercomparison, P.O. Box 808, Mail Stop L-103, Livermore, CA 94550.
E-mail: bonfils2@llnl.gov

DOI: 10.1175/JCLI-D-15-0341.1

1. Introduction

Droughts and floods have profound societal and economic impacts. It is therefore imperative to better understand the mechanisms affecting the mean state and variability of precipitation (P). In the simplest heuristic model, future changes in regional P result from a gradual change in mean seasonal P, which is superimposed upon P teleconnection patterns arising from largely unaltered internal climate variability modes (such as ENSO; Collins et al. 2010).

A number of physical mechanisms have been proposed as contributory factors to the change in mean P in a warmer climate. These include: 1) the "wet-get-wetter"

mechanism (Held and Soden 2006) associated with an increase in tropospheric water vapor; 2) global energy balance constraints, which reduce the percentage increase in global-mean P arising from greenhouse gas (GHG)-induced surface and tropospheric warming (relative to the percentage increase in water vapor caused by the same GHG-driven warming; Allen and Ingram 2002); 3) the poleward displacement of current zonal wet/dry patterns as a result of shifts in atmospheric circulation, which affect the horizontal and vertical transport of water vapor (Marvel and Bonfils 2013; Seidel et al. 2008); and 4) the "warmer-get-wetter" mechanism linking the patterns of tropical SST changes and rainfall changes (with tropical rainfall shifting to regions where the SST increase exceeds the tropical-mean warming; Xie et al. 2010).

Understanding the changes in P variability in a warmer climate is challenging for at least two reasons. First, while most climate models consistently project an increase in the frequency of extreme ENSO events under increased GHG forcing (Cai et al. 2014, 2015; Capotondi 2015), there is considerable model disagreement in projected twenty-first-century changes in the spatial structure and amplitude of ENSO (Coelho and Goddard 2009; Collins et al. 2010; Kao and Yu 2009; Vecchi and Wittenberg 2010). This yields substantial intermodel differences in projected future hydrological changes, both in the tropics and in regions affected by ENSO-driven teleconnections (Meehl and Teng 2007; Kug et al. 2010; Stevenson 2012).

Second, there are also large uncertainties in how ENSO-mediated tropical and extratropical P responses are influenced by GHG-induced changes in the mean state (e.g., spatially nonuniform tropical SST warming) or changes in atmospheric circulation and moisture content (see Huang et al. 2013; Meehl and Teng 2007; Ruff et al. 2012; Seager et al. 2012; Stevenson et al. 2012). The latter issue is important, even if the spatial and temporal characteristics of ENSO are unaltered in the future climate. For example, Watanabe et al. (2014) show that ENSO-induced P variability will increase in the equatorial Pacific under global warming, even in the absence of a robust change in SST variability.

A number of recent studies have relied on single-model AGCM simulations forced with idealized patterns of greenhouse warming and El Niño–induced SST changes. To study the origin of the projected twenty-first-century intensification of El Niño–driven precipitation variability in the central and eastern equatorial Pacific, Power et al. (2013) performed a set of idealized AGCM simulations. They found that the contribution of twenty-first-century changes to the amplitude of ENSO-driven SST variability is secondary compared with nonlinear ENSO responses to mean surface ocean warming. In a complementary study, Chung et al. (2014) showed that the projected tropical Pacific P response to El Niño events strongly depends on the spatial structure of the imposed warming.

Further insights were provided by Zhou et al. (2014), who generated three ensembles of idealized AGCM simulations forced with a 2-yr-long El Niño composite of SST anomalies (see their Fig. 2). Two of these sets of simulations also included an SST warming field that was either spatially uniform or displayed a prescribed pattern. Although the El Niño composite incorporated the full development and decay of an ENSO event, the authors only analyzed the results for the December–February (DJF) season. They found that in both the uniform and nonuniform warming cases, the imposed SST warming substantially reduced the barrier to deep convection in the eastern equatorial Pacific, causing the El Niño–induced P response in DJF to intensify and move eastward. In turn, the shifted anomalies in tropical convection forced the Pacific–North American (PNA) teleconnection pattern to move eastward and intensify. All changes were larger when a nonuniform pattern of SST warming was prescribed. Zhou et al. (2014) confirmed these results using Atmospheric Modeling Intercomparison Project (AMIP) simulations forced by 1) the time-varying observed SST evolution over 1979–2008 (instead of a 2-yr idealized El Niño composite), 2) a superimposed spatially uniform SST increase (amip4K experiments), or 3) a superimposed global spatially patterned SST increase (amipFuture experiments).

In the present study, we use simulation output from fully coupled atmosphere–ocean GCMs to partition future P anomalies into changes in the mean state of P, ENSO-driven P variability, and a future enhancement in the P response to ENSO. We investigate the near-global pattern of P responses to both phases of ENSO using 71 simulations of historical and future climate change from phase 5 of the Coupled Model Intercomparison Project (CMIP5; Taylor et al. 2012). The twenty-first-century climate change results are for representative concentration pathway 8.5. This choice is justifiable because the current carbon dioxide emissions continue to track slightly above this high-end emission pathway (Peters et al. 2013). Splicing the historical simulations (which typically end in December 2005) with the RCP8.5 runs facilitates the comparison with observations over a longer period of the observational record. The spliced CGCM simulations, referred to subsequently as HIST+8.5, encapsulate our best quantitative estimates of future changes in the mean climate state, in the ENSO mode of variability, and in their respective uncertainties (arising from differences in model structure, forcing, and responses).

While use of a large multimodel ensemble is advantageous for identifying robust teleconnection behavior, the diagnosis of results from coupled simulations also presents certain challenges. First, because SSTs in CMIP5 models are predicted instead of prescribed, teleconnection properties are sensitive to intermodel differences in both the mean-state changes and in the amplitude and structure of ENSO-driven SST variability (Coats et al. 2013; Meehl and Teng 2007; Stevenson 2012). Second, certain features of the P response to global warming resemble ENSO-induced P variability (Lu et al. 2008; Marvel and Bonfils 2013), thus complicating the interpretation of simulated P changes. Third, coupled model errors in ENSO characteristics (Capotondi et al. 2015a; Guilyardi et al. 2009) and in the P mean state (Marvel and Bonfils 2013) impact the simulation of ENSO-driven P responses (Coelho and Goddard 2009; Joseph and Nigam 2006; Langenbrunner and Neelin 2013).

Our analysis strategy relies on the identification of a dominant, time-invariant pattern of canonical ENSO (cENSO)[1] SST variability in observations. We are aware that ENSO exhibits a diverse range of spatial patterns, with SST anomalies peaking at different longitudes, as described in an extensive recent literature that is summarized in Capotondi et al. (2015b). However, given the large intermodel spread in present-day ENSO simulations as well as the large uncertainty in projected ENSO changes, we find it useful to focus on one "typical" ENSO pattern. This pattern is then used to study the stationarity and amplitude of P teleconnections, their contribution to future changes in P, and the impact of model quality on the twenty-first-century projections.

Analyzing the underlying thermodynamic and dynamical mechanisms associated with the ENSO-driven P change under global warming is outside of the scope of this study. Instead, based on our single, time-invariant cENSO pattern, we develop a simple common framework useful for determining 1) how well different models capture a key mode of observed internal variability, 2) how the amplitude of this mode evolves in observations and coupled models[2], and 3) whether a better simulation of the observed cENSO pattern translates to improved performance in simulating observed teleconnection behavior. This framework is also useful for decomposing the model-predicted changes in P into different components.

[1] Here the term "canonical" is used to describe "standard" or "typical" ENSO events; it does not imply that the cENSO mode is derived from canonical correlation analysis.

[2] In the idealized experiments, this amplitude is constant, or specified in advance.

2. Datasets and methods

a. Observed cENSO mode

We estimate the cENSO mode by empirical orthogonal function (EOF) analysis of two different observational datasets (section S1): version 3b of the NOAA Extended Reconstructed SST dataset (ERSSTv3b; (Smith et al. 2008) and version 1.1 of the Met Office Hadley Centre Sea Ice and SST dataset (HadISST1.1; (Rayner et al. 2006). We first computed local (grid point) monthly-mean SST anomalies (SSTA) relative to the climatological annual cycle over 1900 to 1909. The choice of the reference period is primarily for visualization purposes and does not affect the main findings of this study. To remove an overall global-scale warming signal and focus attention on internal variability, we subtracted the time-evolving global-mean SSTA (GMSSTA) from the local SSTA, yielding the monthly-mean SST residuals (SSTR). The SSTR and their EOFs have, by construction, an area-weighted spatial average of zero. The cENSO mode (Fig. 1a) is then defined as the leading EOF of the monthly-mean SSTR covariance matrix (for further details, see section S4 in the supplemental material, available online at http://dx.doi.org/10.1175/JCLI-D-15-0341.s1). The cENSO pattern resembles previously described drought-conducive SST anomaly patterns (Capotondi and Alexander 2010; Schubert et al. 2009). The associated cENSO principal component time series (cENSO-PC1; Fig. 1b) is highly correlated with the observed Niño-3.4 index (not shown) with a correlation of $r_{1902–2012} = 0.85$. Performing the EOF analysis using SSTR (instead of using SSTA) better separates the leading mode of ENSO variability from a global-scale warming signal. This signal is evident in the second EOF of SSTR (Figs. 1d,e; see also section S5 and Fig. S1).

b. El Niño life cycle estimated from the observed cENSO mode

Although cENSO is a single time-invariant mode, it can successfully reproduce important aspects of the ENSO life cycle. To illustrate this, the life cycle of El Niño is calculated as the 24-month composite of the cENSO-PC1 time series for five major El Niño events [1972/73, 1982/83, 1987/88, 1997/98, and 2009/10; event selection follows Zhou et al. (2014)]. The composite time series are computed from January of the year of El Niño development (year 0) to December of the year of its decay (year +1). To allow a direct comparison with Fig. 2 of Zhou et al. (2014), which shows the observed time–longitude SST evolution of a typical El Niño event, we projected our 24-month composite onto the spatial average (over 5°N–5°S) of the cENSO pattern at discrete longitudes (in the range 120°E–80°W; see Fig. 1c). By

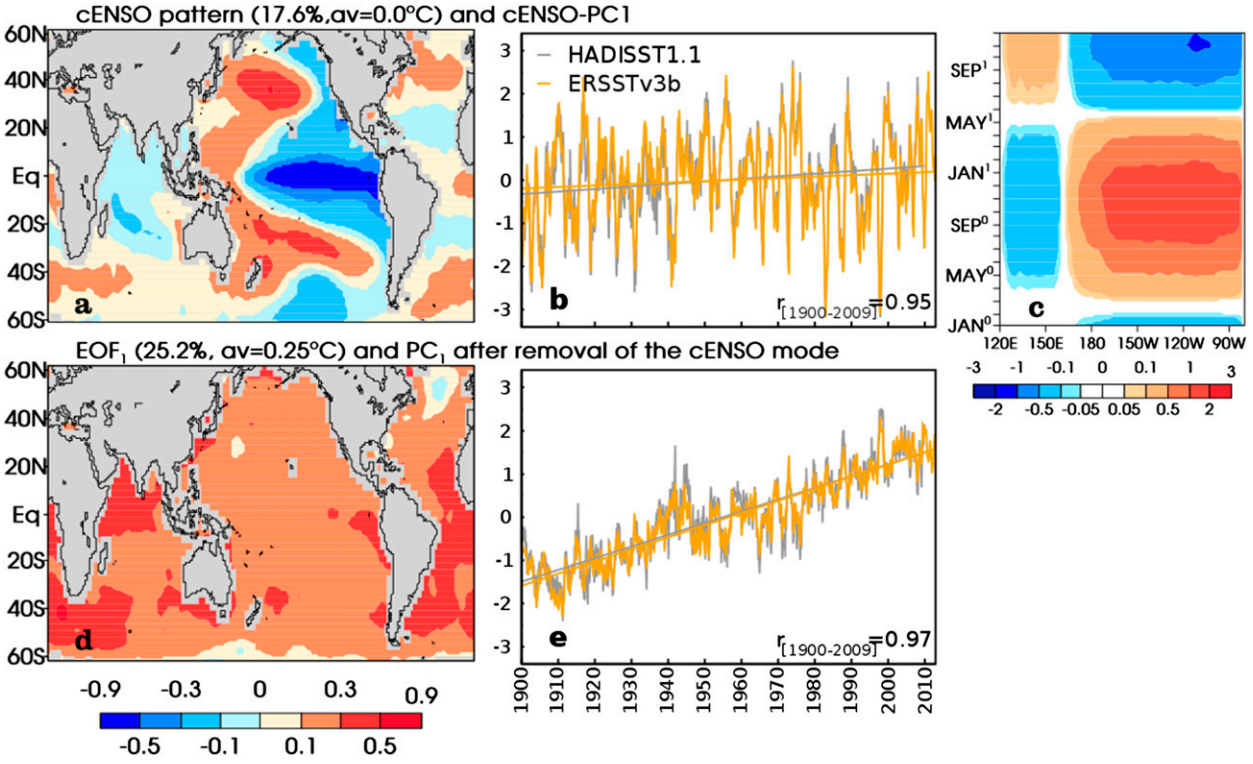

FIG. 1. Leading EOFs (°C) of observed monthly-mean SST anomalies calculated with the ERSSTv3b dataset and associated PCs. PCs for HadISST SST data are also shown. (a) ENSO-like (cENSO) mode calculated using SST residuals (SSTRs), after removal of the global-mean SST anomalies, and (b) the associated cENSO-PC (c) cENSO-based composite analysis of time–longitude section of SST anomalies (°C) showing the development and decay of El Niño events (5°N–5°S mean). The temporal information of this composite analysis is derived from the cENSO-PC_1 time series; the spatial information is derived from the cENSO pattern. (d) Leading mode of SST anomalies after regressing out the cENSO pattern, and (e) the associated PC. The PCs are scaled to have zero mean and unit variance. The spatial patterns are scaled to have °C unit amplitude. For each EOF, the total explained space–time variance of the SSTRs is given (in %), along with the spatial average of the eigenvector. Compared to the ''global-mean included'' case (Figs. S1a,b), the leading modes capturing cENSO and large-scale warming are more clearly separated, and PCs are less sensitive to structural differences between the HADISST1.1 and ERSSTv3b datasets (as expressed by *r* correlation values).

definition, our time-invariant cENSO mode cannot capture the eastward propagation of positive SST anomalies seen in Fig. 2 of Zhou et al. (2014). We note, however, that other aspects of the Zhou et al. ENSO life cycle are well replicated: warm anomalies develop in the central Pacific in summer, peak in winter of year 0, and then decay, followed by a La Niña event in year 1 (Fig. 1c).

c. *Observed cENSO-driven hydrological responses*

We use three different hydrological variables to illustrate the influence of the cENSO mode on regional hydroclimate: 1) column-integrated water vapor over oceans (W), measured by the satellite-based Special Sensor Microwave Imager (SSM/I; Mears et al. 2007); 2) precipitation estimated from the Global Precipitation Climatology Project (GPCP) data (Adler et al. 2003); and 3) the continental Palmer Drought Severity Index (PDSI), calculated using the Penman–Monteith potential evapotranspiration (Dai 2011; Dai et al. 2004). For each variable, anomalies were defined relative to the climatological annual cycle computed over the full observational period of the dataset. We then performed an EOF analysis and identified the leading observed W, P, and PDSI PC time series (see Fig. 2a) that are most highly correlated with the observed cENSO-PC1 [PC1 for W and P and PC2 for PDSI, consistent with Dai et al. (2004)].

To estimate the cENSO-driven hydrological teleconnection patterns, we calculated r_{DJF}, the contemporaneous correlation between the seasonal-mean (DJF only) time series of cENSO-PC1 and the local W, P, or PDSI (Figs. 2b–d). Additionally, we computed $r\{k\}$, which relies on monthly-mean time series for all calendar months (Figs. S2a–c). The lag k is the value of k (in months) that maximizes r at each location. Teleconnections calculated using r_{DJF} and $r\{k\}$ yield very similar results; the latter are primarily influenced by the strong teleconnections in DJF.

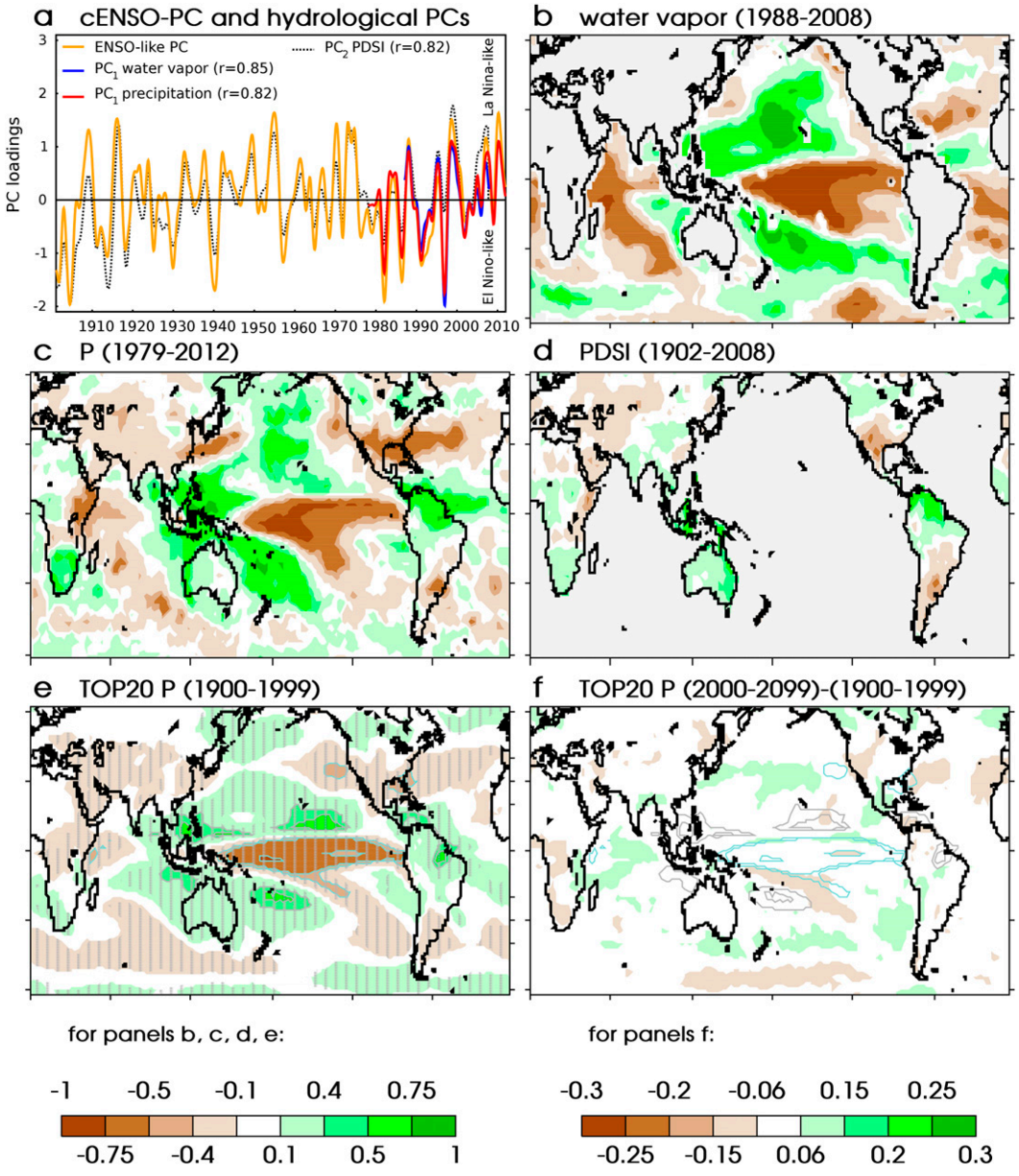

FIG. 2. Observed and simulated hydrological teleconnections driven by temporal variability in the ENSO-like pattern. (a) cENSO PC and most highly correlated PC time series for W (PC_1), P (PC_1), and PDSI (PC_2; 3-month lag). Because of the cENSO-PDSI lag, the PDSI time series is time-shifted by 3 months to facilitate visual comparison of "between variable" covariance relationships. All monthly time series are low-pass filtered. (b)–(d) Observed DJF cENSO-driven W, P and PDSI teleconnection patterns. Each pattern is calculated over the length of the W, P and PDSI observational record. The pattern correlation between (c) and (b) [(c) and (d)] is 0.67 (0.76) over ocean (land). (e),(f) DJF teleconnection patterns averaged over the TOP20 models for the 1900–99 and the difference between the 2000–99 and the 1900–99 periods. Isolines of the teleconnection patterns for the 1900–99 period displayed in (e) (light blue and gray lines) are reproduced in (f). Stippled areas indicate pronounced intermodel agreement ($|S / N| > 1.0$, where S (N) represents the model average (the intermodel standard deviation) of the teleconnection maps).

d. HIST+8.5 simulations

After regridding to a common T42 horizontal grid (see section S3), we analyze model SST and P data from 1) CMIP5 HIST simulations with estimated historical changes in anthropogenic and natural forcings and 2) RCP8.5 simulations forced by projected twenty-first-century changes in GHGs and anthropogenic aerosols.

Model SSTRs were defined as for the observations, with subtraction of each model's local climatological monthly-mean and global-mean SSTA.

For each model, SSTRs were used for two purposes: calculating the model cENSO mode and then projecting onto the observed cENSO mode (Bonfils and Santer 2011). The model cENSO mode calculation allows direct comparison with the observational cENSO pattern (see section S4). The projection of each model's SSTRs onto the observed cENSO pattern yields "pseudo-principal component" time series (not shown), which capture the temporal evolution of the spatial covariance between the observed cENSO pattern and the time-varying model SSTRs. Pseudo-PCs were employed to 1) assess how well models reproduce the observed magnitude of global-scale SST variability associated with cENSO[3] and 2) calculate the model cENSO-driven P teleconnection patterns over the twentieth and twenty-first centuries (Figs. 2e,f; see also Figs. S2d,e and S4). As in the case of the observations, the model P teleconnection pattern is the contemporaneous correlation (or the maximum absolute value of the lagged correlation) between each model's pseudo-PC and its local P time series.

e. Model performance metrics

We used three performance metrics to assess each model's ability to replicate the observed cENSO mode. These metrics gauge the fidelity with which the models represent the spatial structure of the observed cENSO pattern (r_{EOF1}; Figs. 3a and S5a), the amplitude of the observed temporal variability of cENSO-PC1 (σ; Figs. 3a and S5b), and the observed pattern of teleconnections between the variability of cENSO and precipitation (r_{TEL}; Figs. 3b and S5c,d). The r_{EOF1} metric is the centered spatial correlation between the observed cENSO pattern (Fig. 1a) and each simulated cENSO pattern (see Fig. S3). The $\sigma_{1979-2012}$ metric is the temporal standard deviation of the monthly-mean pseudo-PCs, calculated over the 34-yr period of satellite-based SST measurements. Finally, the metric r_{TEL} is the centered[4] spatial correlation between the simulated and observed precipitation teleconnection patterns (Fig. S4). Further details of these metrics are given in section S6 of the supplemental material.

f. Composite analyses

The P teleconnection patterns are estimated by correlating each model's pseudo-PC and its local P time series. Correlations are bounded between -1 and 1, and are insensitive to differences in the amplitude of the two time series being correlated.[5] We therefore decided to use a composite analysis of ENSO events [as in Stevenson (2012) and Meehl and Teng (2007)] to investigate changes in the amplitude of the P response to ENSO events. Two types of composite analyses (CA) were performed in this study. For each CA and each simulation, large La Niña–like and El Niño–like events were identified from the detrended model pseudo-PC time series, using an amplitude threshold of >1 or <-1, respectively. We then averaged the corresponding DJF P response for each set of events. The P anomaly time series were not detrended in composite analysis 1 (CA1) but were in composite analysis 2 (CA2). Over the 1900–99 period, the two composites yield very similar results, because the P time series show relatively small trends over this period. Over the 2000–99 period, however, CA1 (Fig. 4a) captures both the change in P mean state (Fig. 4c) and any change in the ENSO-induced variability of P (Fig. 4b). In contrast, CA2 largely reflects the cENSO-driven P variability. By comparing the results of CA2 for the 1900–99 and the 2000–99 periods, we can identify a change in cENSO-driven P variability between the two centuries (Fig. 4d). Seager et al. (2012) used a similar technique to determine whether global warming causes intensified interannual variability in the difference of precipitation and evaporation ($P - E$).

3. Results

a. Observed teleconnections

To account for the pronounced seasonality of ENSO teleconnections, and to compare our results with those of

[3] Pseudo-PCs are often used in pattern-based detection and attribution studies, in which a model-predicted anthropogenic fingerprint is searched for in observations (see, e.g., Santer et al. 2009). They also have been used to investigate the aliasing of a large-scale anthropogenic warming signal in the Pacific decadal oscillation index (Bonfils and Santer 2011) and to assess model quality in simulating the Madden–Julian oscillation (Sperber and Kim 2012). Sperber et al. (2005) have noted that use of different basis functions (e.g., leading EOFs estimated separately from observations and individual models) can hamper interpretation of intermodel and model-versus-observational differences. In contrast, projecting observational and model data onto a common basis function—as we do here—facilitates the direct comparison of modeled and observed teleconnection behavior. We are not aware of any other paper in the literature that uses pseudo-PC time series to calculate P teleconnections.

[4] The centered statistic measures the similarity of two patterns after removal of their spatial means.

[5] In consequence, amplification of the P response to ENSO events in the twenty-first century does not necessarily yield larger absolute values of the correlation coefficients.

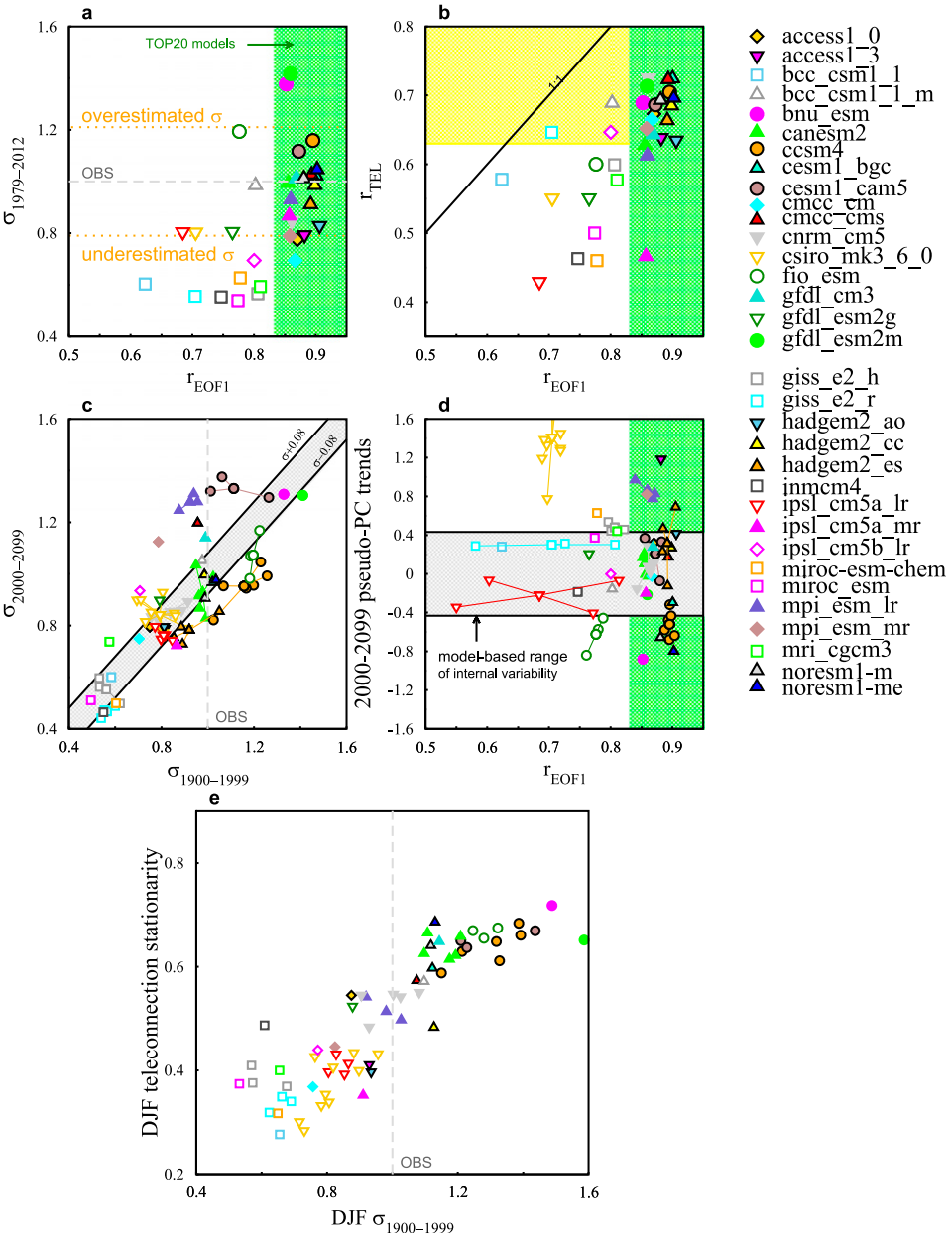

FIG. 3. Relationship between model skill in simulating the observed cENSO pattern (as measured by the r_{EOF1} metric) and (a) model skill in simulating observed cENSO variability σ_{OBS} and (b) the observed teleconnection patterns, r_{TEL} (based here on all calendar months). (c) Relationship between the amplitude of twenty-first- and twentieth-century cENSO variability (both calculated as the temporal standard deviation of the detrended monthly-mean pseudo-PC time series). (d) Relationship between the model skill in simulating the observed cENSO pattern and the overall model-simulated cENSO changes in the twenty-first century. (e) DJF teleconnection stationarity, measured as the centered spatial correlation between the P teleconnection patterns for the 1900–99 and 2000–99 periods. Metrics displayed in (a) and (b) are the realization-ensemble mean statistic for each model (see Table S1). Data in (c)–(e) are displayed for each individual realization. The TOP20 models are represented with solid symbols. The gray shading in (d) represents the two-tailed 95% confidence interval of internal variability, calculated as $\varepsilon \times 1.96$, where ε is the standard error of the sampling distribution of 100-yr overlapping unforced trends in the TOP20 control runs (with overlap = 10 yr). The green shaded areas in (a),(b), and (d) denote r_{EOF1} values > 0.83, the cutoff for definition of the TOP20 models, while the yellow shaded area in (b) indicates the 20 models that best reproduce the observed teleconnections (based on the r_{TEL} metric). The orange dotted lines in (a) delimit the 20 models that best reproduce the observed $\sigma_{1979-2012}$, as shown in Fig. S5b of the supplementary online material.

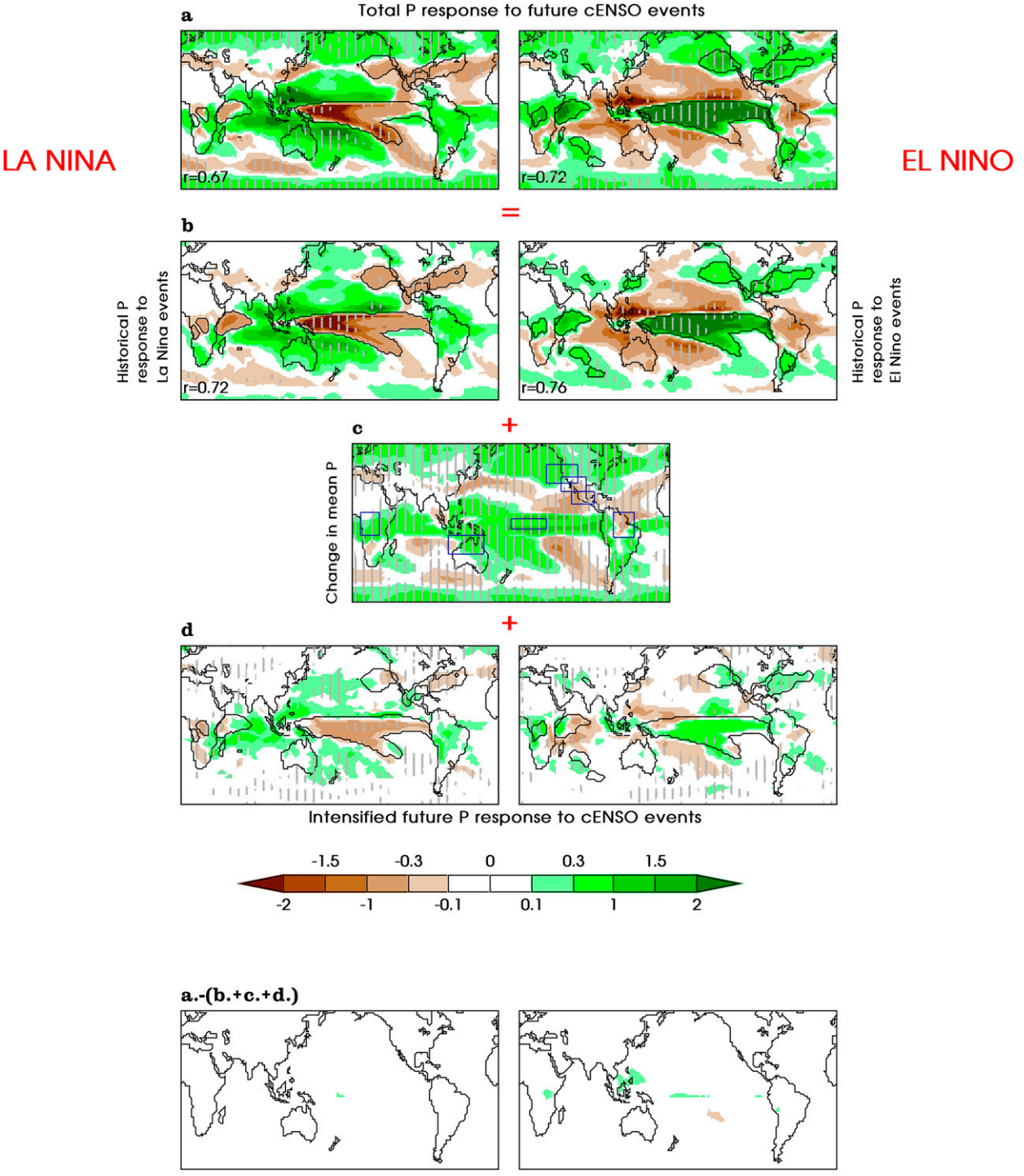

FIG. 4. Decomposition of the total DJF precipitation response (mm day^{-1}) to future cENSO events using the TOP20 models. (a) Future (2000–99) and (b) present-day (1900–99) *P* anomalies (both relative to the same historical baseline) in response to La Niña– and El Niño–like events (based on the CA1 technique; see text). The respective spatial correlations with the GPCP-based composite maps (computed over the 1979–2012 period) are indicated in the left corner of the panels. (c) Change in mean DJF *P* (this panel is independent of the ENSO phase). Note that rectangles mark areas for further regional analysis; see Fig. 7. (d) Enhanced future *P* response to La Niña– and El Niño–like events from CA2 (see text). This amplification component is the difference between future and the present-day *detrended P* composites. Vertical strips highlight regions with statistically significant differences under a two-sided *t* test at a 10% level, with a sample size of 20 models.

idealized AGCM experiments, our analysis (unless otherwise indicated) focuses on DJF, the peak season of ENSO impact. Figure 2a shows that the cENSO-PC is highly correlated with the leading PC of column-integrated water vapor over oceans ($r_{[1988–2008]} = 0.85$) and PC1 of precipitation ($r_{[1979–2012]} = 0.82$), as well as with the second PC of the continental PDSI ($r_{[1902–2008]} = 0.82$). In terms of the spatial patterns of these relationships, we find that extensive areas of the tropics are characterized by strong negative and positive correlations between cENSO variability and changes in hydroclimate (Figs. 2b–d). Despite differences in measurement platforms, instrumentation, spatial coverage, and the length of the observational record, the teleconnection patterns in the *P*, *W*, and PDSI fields are very similar (Figs. 2b–d). This clearly illustrates that the temporal behavior of the cENSO pattern has a broad influence on a variety of interrelated aspects of hydroclimatic variability (Dai and Wigley 2000; Dai et al. 2004; Trenberth et al. 2005).

In the positive phase of the cENSO pattern (corresponding here to a La Niña event), the colder central-eastern equatorial Pacific is associated with reduced precipitation, while enhanced precipitation occurs in the far western Pacific and over the Maritime Continent (Fig. 2c). Over land, drier conditions prevail across southern North America, East Africa, and southern South America, while wetter conditions are found in northern South America, southern Africa, southwest India, and some parts of Australia, in agreement with results from previous studies (e.g., Dai and Wigley 2000).

b. Model performance evaluation

We first employ the r_{EOF1} metric to identify the models with the best representation of the observed cENSO pattern. The r_{EOF1} values span the range 0.62 to 0.91; the associated model rankings are given in Fig. S5a. We use the ranked r_{EOF1} results (Fig. S5a) to select the "TOP20" models ($r_{EOF1} > 0.83$[6]). Since model errors are complex functions of space, time, and variable (see, e.g., Santer et al. 2009), alternate metric choices would likely yield different model rankings. For our specific application, however, model performance in representing the observed cENSO pattern is of primary importance for accurate simulation of cENSO-driven teleconnection patterns. This provides considerable justification for our use of r_{EOF1} to select better performing models.

The TOP20 models are markedly more successful in reproducing both the observed amplitude of cENSO temporal variability ($\sigma_{1979–2012}$, Fig. 3a) and the cENSO-driven *P* teleconnection patterns (r_{TEL}), irrespective of whether these metrics are calculated using all months (Figs. 3b) or all DJFs of the pseudo-PCs (Fig. S5e). For example, in both the "all months" and "individual DJF" cases, 17 of the models that best capture the observed r_{TEL} pattern are in the TOP20 set. Similarly, most models that produce a pseudo-PC time series with temporal variability that is smaller than observed are also unable to satisfy the TOP20 r_{EOF1}-based criterion (Fig. 3a).[7]

c. Changes in cENSO

Models that perform well in reproducing the spatial structure of the observed cENSO pattern (r_{EOF1}) also tend to display larger amplitude of cENSO and Niño-3.4 variability for the historical period. We note, however, that the r_{EOF1} metric does not help to reduce the spread of model results in the change in amplitude of the twenty-first-century temporal variability of the cENSO pattern (Fig. 3c). The TOP20 models (all denoted by solid symbols) do not project a robust increase or reduction in cENSO variability. A comparison of the twentieth- and twenty-first-century results indicates that five TOP20 models project an increase in magnitude of the cENSO variability (CESM1-CAM5, CMCC-CMS, GFDL CM3, MPI-ESM-LR, MPI-ESM-MR; see http://www.ametsoc.org/PubsAcronymList for expansions of model names), five models project a reduction in cENSO variability (CCSM4, GFDL ESM2M, HADGEM2-ES, IPSL-CM5A-MR, NORESM1-M), and 10 models display no appreciable change (ACCESS1.0, ACCESS1.3, BNU-ESM, CanESM2, CESM1-BGC, CMCC-CM, CNRM-CM5, HADGEM2-AO, HADGEM2-CC, NorESM1-ME). Most models that are not included the TOP20 group underestimate the observed temporal variability of the cENSO PC in the twentieth century, and continue to project low pseudo-PC variability in the twenty-first century (Fig. 3c).

[6] The choice of 20 models is motivated by Fig. S5a, which naturally separates the models into two groups: those with $r_{EOF1} > 0.83$ and with relatively small intermodel correlation differences, and those with much lower r_{EOF1} values. We did not use other criteria to select the "best" models.

[7] Relatively low temporal variance in the pseudo-PC may occur because of two factors: 1) the observed tropical Pacific variability is underestimated in the model of interest and/or 2) the simulated amplitude of tropical Pacific variability is realistic, but there are substantial spatial biases in the model SST fields, which result in poor projection of the simulated SSTR fields onto the observed cENSO pattern. The strong correlation across realizations between the amplitude of the variability of pseudo-PCs and Niño-3.4 time series (Fig. S5f) suggests that the simulated tropical Pacific SST variability is the main driver of the temporal variance in the pseudo-PCs. This supports hypothesis 1 above.

The observed cENSO pattern and all simulated SSTRs have an area-weighted spatial average of zero (see section 2a). By definition, therefore, trends in the cENSO pseudo-PCs are insensitive to spatially uniform ocean warming, but should be sensitive to warming with a spatial structure resembling the cENSO SST pattern itself (section S5). Trends in the cENSO pseudo-PCs over 2000–99 do not show consistent behavior across the CMIP5 models (Fig. 3d). This appears to contradict results from several previous studies, which found that most CMIP5 models tend to produce more El Niño–like conditions in the twenty-first century (Bayr et al. 2014), with faster warming in the tropical eastern Pacific relative to the entire tropical Pacific basin (Power et al. 2013; Zhou et al. 2014). We hypothesize that this apparent contradiction arises from the effects of intermodel differences in extratropical SST variability (which are projected onto the cENSO pattern) rather than from the lack of a consistent El Niño–like mean SST warming pattern in response to increasing GHGs.

d. *Spatial stationarity of ENSO-driven* P *patterns*

For the TOP20 case, the multimodel average ENSO-driven P teleconnection pattern reproduces many key features of the observed pattern (Figs. 2c,e; Figs. S2b,d). This holds for calculations involving DJF only and all calendar months. The multimodel average P pattern in the TOP20 models (Fig. 2e) has smaller amplitude features than the corresponding observed pattern (Fig. 2c). This is mainly due to such factors as spatial smoothing (arising from averaging of results over realizations and models) and to intermodel differences in the spatial features of the teleconnection patterns, rather than to a muted P response in each individual model (Fig. S4). The simulated teleconnection patterns for the twentieth and twenty-first centuries (which are both calculated relative to the twentieth- and twenty-first-century mean states, respectively) are almost identical in the ''all calendar months'' calculations (Fig. S2e). This result implies that the cENSO-driven P teleconnection spatial patterns estimated from the TOP20 multimodel ensemble are largely stationary.

Over the DJF season (when ENSO-mediated P variability is most pronounced), the multimodel average P teleconnection patterns are very similar in the twentieth and twenty-first centuries (Figs. 2e,f; $r_{1900–1999/2000–2099} = 0.95$). When analyzed individually, however, the models (Fig. S4) show a large spread in the spatial similarity between their twentieth- and twenty-first-century teleconnection patterns.

The spatial stationarity of DJF patterns is most pronounced in models with a large amplitude of DJF pseudo-PC variability in the twentieth century (Fig. 3e). In contrast, models that underestimate temporal variability of the observed cENSO pattern yield spatial DJF teleconnection patterns that are less stationary and more easily disrupted by other sources of internal variability (Coats et al. 2013). This suggests that the spatial stationarity metric is sensitive to the amplitude of cENSO events, which affects the degree to which deep convection is triggered in the tropical Pacific region (not shown), and thus the strength of the atmospheric teleconnections.

e. *Amplification of the cENSO-driven* P *responses*

In this section, we examine the individual components that contribute to the projected changes in twenty-first century P anomalies in response to ENSO variability (see Figs. 4 and S6). We first apply composite analysis 1 (section 2e), identifying all large La Niña–like and El Niño–like events from the model pseudo-PCs, and then averaging the corresponding total (i.e., nondetrended) DJF P response for each set of events. Over the 1900–99 period, this analysis shows that the TOP20 models reliably capture many of the features of the observed pattern of P response to cENSO variability (Fig. 4b). When CA1 is performed over the 2000–99 period (Fig. 4a), these features of the twentieth century teleconnection pattern are still visible, but they are also imprinted with the change in the mean DJF P between the twentieth and twenty-first centuries (Fig. 4c). This change in mean state is spatially complex. It is influenced by further moistening of the currently wet areas of the tropics and storm-track regions, and by further drying of currently dry portions of the subtropics. This behavior is typically associated with the ''wet-get-wetter'' mechanism; (Held and Soden 2006; Huang et al. 2013). The pattern of mean state change also reflects increased rainfall over the equator relative to the southeast tropical Pacific, which is consistent with the ''warmer-get-wetter'' mechanism (Huang et al. 2013).[8]

Assuming a linear response of P to the future behavior of ENSO, the total P associated with future ENSO events (Fig. 4a) should be well described by summing the historical P responses to cENSO variability (Fig. 4b) and the change in mean P (Fig. 4c). However, a number of AGCM-based studies (e.g., Chung et al. 2014; Huang et al. 2013; Power et al. 2013; Zhou et al. 2014) suggest that such a simple partitioning of the P response

[8] One caveat is that some component of the mean change in P could also be a result of ENSO-driven changes in the variability of P. Examples of such behavior might involve a change in the relative frequency of El Niño and La Niña events, or enhancement of the precipitation response to El Niño events (relative to La Niña events).

provides an inadequate explanation for the projected changes in P. Since deep convection responds to SST thresholds, changes in equatorial SSTs due to global warming are expected to alter the atmospheric response to ENSO, even in absence of significant changes in twenty-first-century ENSO events. To estimate this nonlinear contribution to the total P response in the CGCMs, we followed the approach of Seager et al. (2012), and detrended both the model pseudo-PCs of SST and the model P data prior to constructing composites (CA2). In most regions, the difference maps between the twentieth- and twenty-first-century composites reveal an amplified P response to both El Niño and La Niña phases (Fig. 4d). In the El Niño case, the intensification is more pronounced in the central-eastern Pacific.

Is the amplified response solely caused by a projected change in the amplitude of ENSO-driven SST variability? To address this question, we estimated the nonlinear "missing term" using the three sets of models—those showing an increase ($\sigma_{\uparrow}$), a decrease ($\sigma_{\downarrow}$) or no discernible projected change ($\sigma_{\rightarrow}$) in the amplitude of pseudo-PC variability between the twentieth and twenty-first centuries. The results are displayed in Fig. 5. We find that the P variability is projected to intensify, even in absence of a change in cENSO amplitude (the $\sigma_{\rightarrow}$ case). The amplification of P variability, however, is also modulated by the projected change in the magnitude of σ: it is larger in simulations where σ is projected to increase ($\sigma_{\uparrow}$) and damped in simulations where σ is projected to decrease ($\sigma_{\downarrow}$).

When near-future (2017–50) and more distant future (2059–92) 33-yr[9] periods are compared (Figs. S7 and S8), it is evident that both the magnitude of the mean P change (Figs. S7c and S8c) and the amplification components (Figs. S7d and S8d; see also Fig. 5) become larger as the tropical mean SST warming increases and the GHG-forced global atmosphere becomes warmer and moister.

Consistent with previous findings, the TOP20 models show that the center of action of wintertime cENSO-driven P responses is projected to shift eastward in the equatorial Pacific and near the North American Pacific west coast (cf., e.g., Figs. 4b and 4d for the El Niño case). To better understand this result, we compute, after Power et al. (2013), the P anomalies along the equator for the El Niño case. Comparison of the solid and dashed black lines in Fig. 6a reveals that the amplification component in the eastern tropical Pacific is accompanied by a clear eastward shift of the positive P anomalies. This shift, which occurs even in the $\sigma_{\rightarrow}$ simulations (blue lines) is accentuated in the $\sigma_{\uparrow}$ simulations (red lines), but is reduced in the $\sigma_{\downarrow}$ simulations (green lines). During La Niña events, the negative P anomalies intensify in the central Pacific in all cases ($\sigma_{\rightarrow}$, $\sigma_{\uparrow}$, $\sigma_{\downarrow}$). The twenty-first-century negative P anomalies in the eastern tropical Pacific (east of 160°E) are also located eastward of their historical counterparts, especially in the $\sigma_{\uparrow}$ simulations (red lines), as compared with the $\sigma_{\downarrow}$ simulations (green lines). Given that the eastern equatorial Pacific is typically dry, except during El Niño events, the changes depicted in (b) are likely related to changes in the climatology, which in turn are related to the changes during El Niño events (see Fig. 6a, which shows little change in the green lines, and the greatest change between the red lines). Similar results from the North Pacific region are discussed in the next section.

4. Discussion

a. Mechanisms

As noted in the previous section, future DJF precipitation responses to ENSO-like events can be decomposed into the sum of three components: 1) a mean-state change in P, 2) the historical P anomalies in response to cENSO variability, and 3) a component capturing the future amplification and locational shift of the historical P anomalies associated with ENSO (Fig. 4). Although component 3 is affected by model uncertainties in σ (the amplitude of the twenty-first-century variability in the cENSO pseudo-PCs), this component amplifies the cENSO-driven P variability in most regions (Fig. S9) and increases the magnitude of cENSO-driven extreme dry/wet anomalies at locations already sensitive to ENSO events.

Several different mechanisms can be invoked to explain why the P responses to El Niño and La Niña are projected to intensify and shift eastward in the future. First, the Held and Soden (2006) wet-gets-wetter mechanism in a warmer and moister atmosphere does not operate exclusively on climatologically wet and dry features. This mechanism can also impact regions that are affected by ENSO and are experiencing either anomalously wet or dry conditions. The net effect is to further enhance wetting or drying of these regions, depending on the ENSO phase. Second, the mean SST warming and the detailed spatial pattern of the projected warming in the tropical Pacific (e.g., Chung et al. 2014; Zhou et al. 2014) both seem to play a major role in triggering the eastward shift and intensification of 1) the

[9] The 33-yr analysis time scale is determined by the length of the GPCP observational dataset (which spans the period from 1979 to 2012). The two selected analysis periods are 38 years and 80 years after the beginning of the observational period.

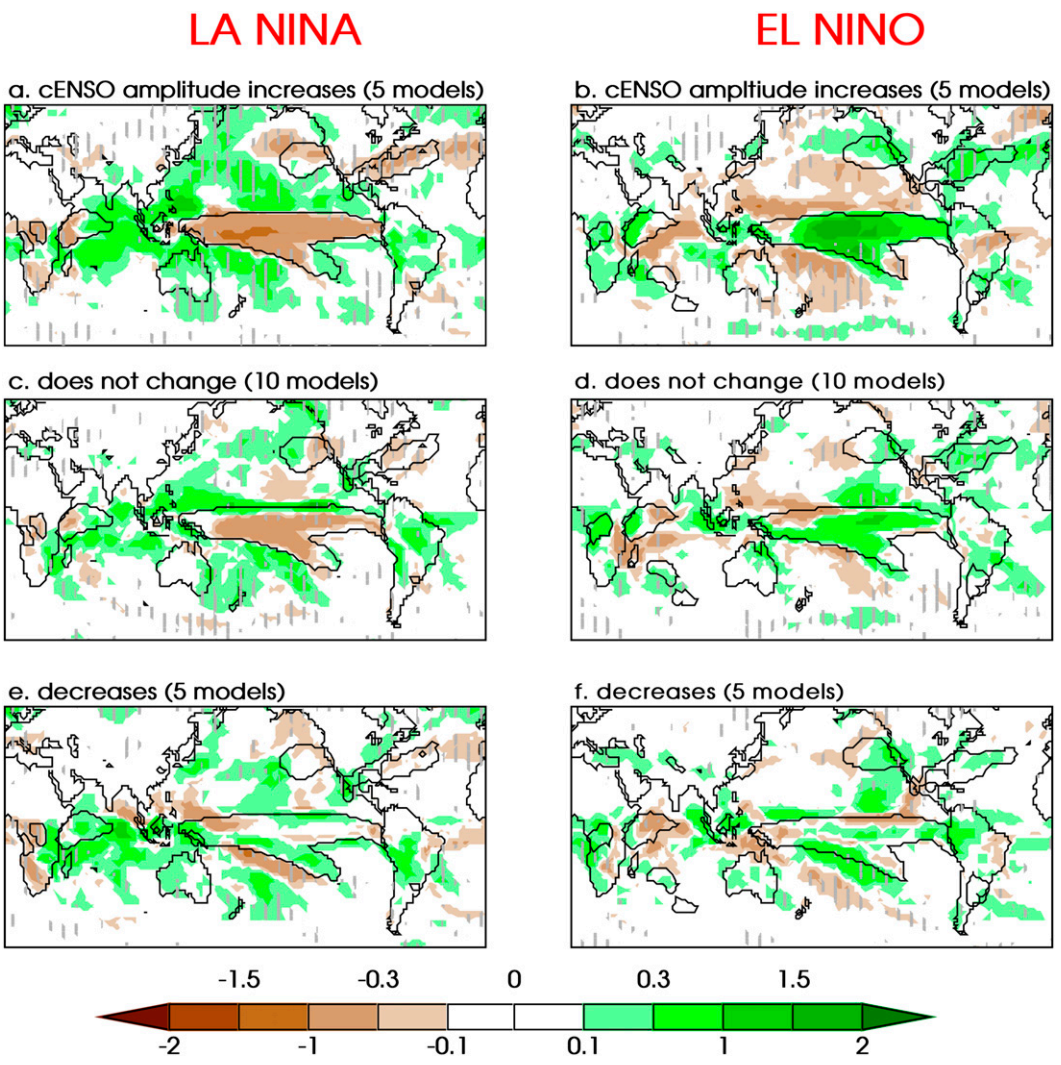

FIG. 5. Amplification components, as in Fig. 4d, calculated from model subsets projecting an increasing, unchanged, and decreasing amplitude (respectively) of SST cENSO variability. Vertical strips highlight regions with statistically significant differences under a two-sided *t* test at a 10% level, with a sample size of 5, 10 and 5 models, respectively.

main convection centers in the tropics (Figs. 6a,b) and 2) the teleconnected *P* responses in the North American sector (Figs. 6c,d).

Climatologically, the eastern Pacific is dry and cool, whereas the easterly trade winds drive warm water toward the western Pacific and create favorable conditions for upwelling of cold water in the east Pacific. The twenty-first-century anthropogenic warming signal in most CMIP5 models tends to be larger in the eastern equatorial Pacific than in the surrounding ocean waters (according to Bayr et al. 2014; Cai et al. 2014; Power et al. 2013). This asymmetric pattern of temperature change has been identified in coupled climate simulations (Vecchi et al. 2006) and is consistent with the weakening of the Walker circulation and surface easterly winds under global warming. The resulting reduction of the zonal SST gradients along the equator weakens the barrier preventing eastern Pacific SST from triggering deep convection. In these conditions, even a small increase in SST can significantly alter atmospheric convection and favor a shift and intensification of *P* in the tropical eastern Pacific during warm events. Thus, if ENSO amplitude does not increase with global warming, the superposition of warm El Niño SST anomalies and the warmer background conditions can lead to an eastward displacement of convection and an increased frequency of extreme El Niño events (Cai et al. 2014; Chung et al. 2014; Kug et al. 2010; Power et al. 2013; Zhou et al. 2014).

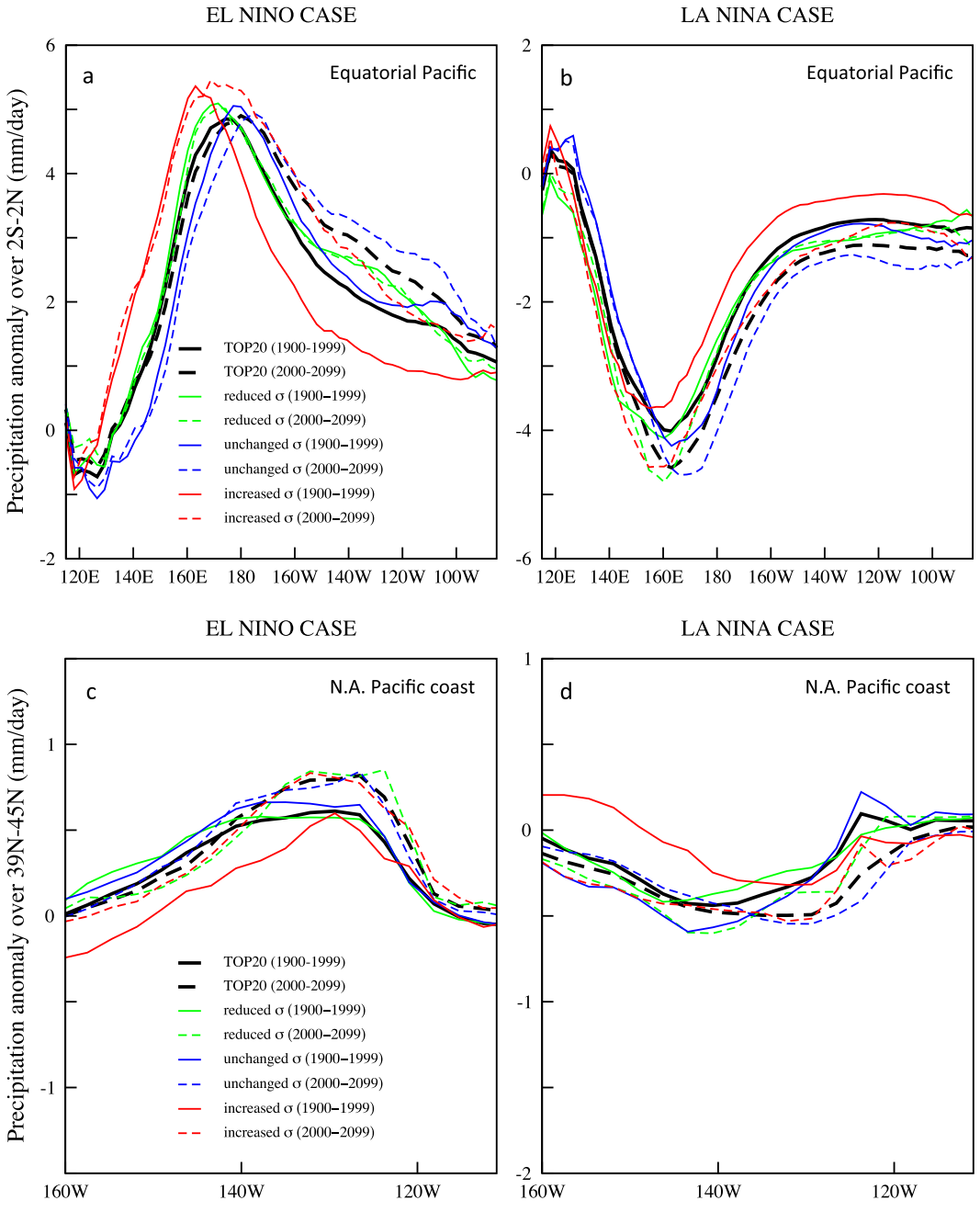

FIG. 6. DJF precipitation (a),(b) along the equator (2°S–2°N) and (c),(d) at the North American Pacific West Coast (39°–45°N), during El Niño and La Niña events. Results are computed for the TOP20 models, and for the three sets of models classified by the magnitude of temporal variability of the cENSO pseudo-PC (σ). The zonal means are computed from the precipitation composites used to create Figs. 4d and 5, based on detrended cENSO and P fields. The multimodel average of σ over 1900–99 is 1.07 (0.96) when calculated using the 5 (5) models projecting a decrease (increase) in SST cENSO magnitude, and 0.93 when computed using the models with no discernible change in σ.

Extreme La Niña events are also projected to become more frequent, as explained in Cai et al. (2015) and Capotondi (2015). During normal La Niña events, trade winds intensify and cause the central Pacific to become colder and drier, resulting in a westward shift of deep convection. These features are enhanced during extreme La Niña events, and deep convection shifts farther west toward the Maritime Continent. Anthropogenic warming is projected to increase faster over the landmasses in the Maritime Continent than in the central

equatorial Pacific, resulting in an enhanced SST gradient between these two regions. As a consequence, the anomalous trade winds become stronger in the area where the SST gradient increases, displacing water westward and poleward and leading to enhanced upwelling. Because of the increased vertical temperature gradient (with surface waters warming faster than deeper water) the latter process will produce relatively colder anomalies in the central Pacific and will further increase the temperature gradient between Maritime Continent and the central Pacific, favoring the development of extreme cold events. In the twenty-first-century simulations, the enhanced reduction of precipitation in the central-eastern Pacific during La Niña events (Fig. 6b) is consistent with the projected increase in the frequency of extreme La Niñas.

In the middle and high latitudes, the climate responses to ENSO events strongly depend on the locations of tropical atmospheric convection centers, which affect the propagation pathways of atmospheric waves. In comparing idealized control and $2\times CO_2$ simulations from eight CMIP3 models, Kug et al. (2010) show that 1) tropical Pacific SST increases resulting from GHG warming promote the eastward shift of the main tropical convections centers associated with both El Niño and La Niña (in accord with our results) and 2) the eastward shift of tropical convection anomalies results in systematic eastward shifts in the midlatitude DJF precipitation teleconnection pattern, again during both ENSO phases. In the North American sector we find a similar eastward shift of P anomalies in response to both El Niño and La Niña in the $\sigma_{\rightarrow}$ and $\sigma_{\downarrow}$ cases (Figs. 6c,d). In the $\sigma_{\uparrow}$ case, the increase (decrease) in P anomalies in response to El Niño (La Niña) occurs at all longitudes. The analysis of Zhou et al. (2014), which is most comparable to the to our $\sigma_{\rightarrow}$/El Niño case, yields analogous results, with the spatial pattern of tropical SST warming producing larger teleconnections changes than a spatially uniform warming.

b. *Three-term decomposition*

With few exceptions (Watanabe et al. 2014; Wittenberg 2015), most previous studies focus on individual components of projected P changes: the change in mean P, the historical P variability, or the change in P variability (i.e., the nonlinear term). Here, we consider the combined effects of these three components on regional scales. Because changes in mean and variability are both spatially complex, it is difficult to intuitively predict how the total P anomalies will behave in a particular region (relative to some historical reference).

Our simple three-term decomposition framework provides a quantitative estimate of the relative importance of each of these terms in different geographical regions (Fig. 7). It also helps to identify regions where the projected twenty-first-century P responses to cENSO variability are without precedent in the current climate. For example, an amplified P response to both cENSO phases is projected over the northeastern Pacific region. Here, however, the future P response to La Niña lies within the range of historical variability, while the future response to El Niño is projected to be outside of the range of historical P responses. In the southwestern United States, the dry conditions in response to future La Niña events are projected to be outside of the range of historical P responses. In contrast, the change in mean P over Mexico always yields drier than historical conditions, independent of the cENSO phase. These three examples illustrate that reliable assessment of flood and drought risk in the future must rely on estimates of all three components discussed here.

5. Conclusions

Future ENSO-driven P responses are sensitive to changes in both the mean state of P and to changes in the amplitude and structure of ENSO-driven P variability. To investigate how ENSO-driven P variability may change in a warming climate, many previous studies have relied on single-model AGCM simulations forced with idealized greenhouse warming patterns, and/or with an idealized El Niño–induced SST pattern (with predetermined amplitudes) superimposed on some predetermined global-mean SST change. In this study, we rely instead on CGCM multimodel HIST+8.5 simulations. Here, we seek to 1) identify a time-invariant canonical ENSO (cENSO) pattern in observed SST data; 2) project the simulated SSTs onto the observed cENSO mode; 3) sort the simulations according to whether they produce an increase, a decrease, or no significant change in the magnitude of the cENSO variability in the twenty-first century; 4) calculate various measures of model performance in capturing observed cENSO characteristics, and observed teleconnection relationships between temporal variability in the cENSO pattern and local P; and 5) develop a simple heuristic model to partition twenty-first-century P changes into mean state and variability components.

We find that CGCMs with better representation of the structure and variability of the observed cENSO produce rainfall teleconnection patterns that are in better accord with observations. We hypothesize that simulations with larger amplitude cENSO variability trigger deeper convection in the tropical Pacific region, thereby forcing atmospheric teleconnection patterns that remain

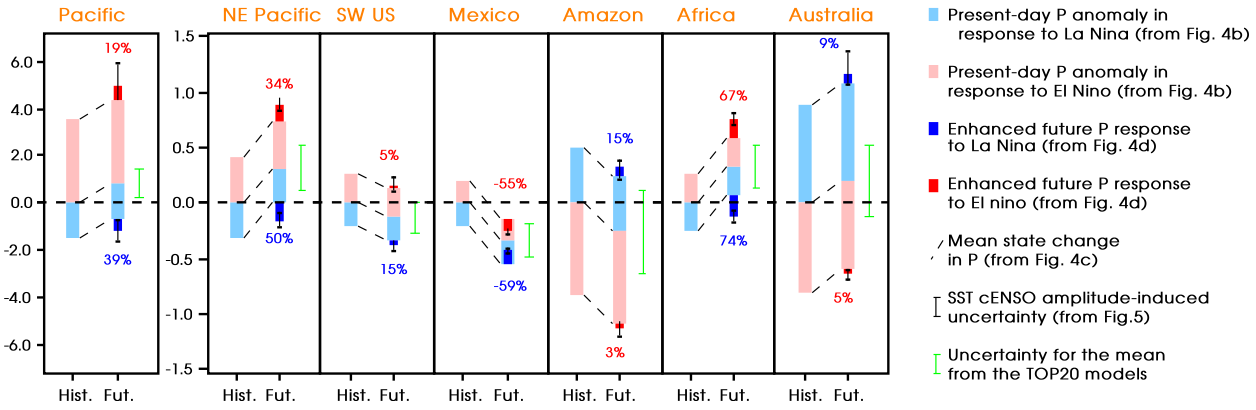

FIG. 7. Regionally averaged historical and future P anomalies in response to cENSO events in the seven regions indicated by the rectangles in Fig. 4c. The future cENSO-driven P anomalies can be decomposed into a change in the P mean state (dashed lines, calculated from Fig. 4c), the historical cENSO-driven P response (the light blue and red boxes, calculated from Fig. 4b), and the amplification of this historical P response (the dark blue and red boxes, calculated from Fig. 4d) (also expressed in % of the historical response). The whiskers represent the model uncertainties in changes in the amplitude of cENSO-driven SST variability (from Fig. 5).

more stationary through time (section 3d). Finally, we find that most regions of the globe exhibit enhanced anomalies in future P as a response to both El Niño– and La Niña–like phases. This change in P is accompanied by a clear eastward shift of teleconnection patterns in the equatorial Pacific and in the North Pacific, which occurs even in the absence of a robust increase in cENSO variability amplitude.

Our study investigates the effects of a time-invariant, observationally derived ENSO pattern on the geographical pattern of P anomalies. This relationship is explored in the context of both twentieth- and twenty-first-century climate change. Although our focus is specifically on this canonical ENSO mode, it is clearly possible that other natural modes of SST variability might alter existing teleconnections between SST and P. It is beyond the scope of this paper to consider how ENSO-driven P responses might be affected by 1) a change in the SST structure of ENSO, including the recent prevalence of central-Pacific over east-Pacific El Niño events (Yeh et al. 2009); 2) GHG-induced changes in other modes of variability; and 3) a seasonal shift in the ENSO life cycle. Such issues merit further investigation.

As discussed in section 4, the amplification of the ENSO precipitation response in the eastern Pacific and the corresponding eastward shift of the precipitation pattern may be associated with a projected enhanced warming trend in the eastern equatorial Pacific. This pattern of warming may result from a weakening of the Walker circulation seen in some models (Vecchi et al. 2006) and in observations (Tokinaga et al. 2012). However, this view has been challenged by other observational studies (L'Heureux et al. 2013; Sandeep et al. 2014), which suggest that the Walker circulation may instead have strengthened over the past century. This strengthening is consistent with a cooling trend found in the eastern Pacific in several observational SST datasets after statistical removal of the ENSO mode (Compo and Sardeshmukh 2010; Karnauskas et al. 2009; Solomon and Newman 2012).[10] There remain, therefore, important uncertainties in the projected changes in SST and precipitation, as well as in their causes. Reducing uncertainties in projections of twenty-first-century ENSO behavior and related teleconnections may require several decades of research. Despite these significant uncertainties, our study establishes a useful conceptual framework for decomposing and analyzing projected changes in regional precipitation. This framework may help to inform important current and future decisions regarding food security and water resource management.

Acknowledgments. We acknowledge the World Climate Research Programme's Working Group on Coupled Modelling, which is responsible for CMIP, and we thank the climate modeling groups (listed in Table S1 of this paper) for producing and making available their model output. For CMIP the U.S. Department of Energy's Program for Climate Model Diagnosis and Intercomparison provides coordinating support and led development of software infrastructure in partnership with the Global Organization for Earth System Science Portals. CMIP5 data processing was enabled by the CDAT analysis package. A. Dai (University at Albany)

[10] Likewise, Fig. 1b shows a positive trend in the cENSO-PC$_1$ time series over the instrumental interval, which is consistent with a recent shift toward more La Niña–like conditions.

calculated the second PC of the PDSI dataset (as in Fig. 2d). This work was supported by the Climate and Environmental Sciences Division (CESD) and the Regional and Global Climate Modeling (RGCM) Program of the U.S. Department of Energy (DOE) Office of Science and was performed under the auspices of the U.S. DOE Lawrence Livermore National Laboratory (Contract DE-AC52-07NA27344). K.M. was supported by a Laboratory Directed Research and Development award (13-ERD-032). C.B. was fully supported by the DOE/OBER Early Career Research Program Award SCW1295. We thank our three reviewers for their very helpful and constructive comments, which have substantially improved our paper.

REFERENCES

Adler, R., and Coauthors, 2003: The version-2 Global Precipitation Climatology Project (GPCP) monthly precipitation analysis (1979–present). *J. Hydrometeor.*, **4**, 1147–1167, doi:10.1175/1525-7541(2003)004<1147:TVGPCP>2.0.CO;2.

Allen, M., and W. Ingram, 2002: Constraints on future changes in climate and the hydrologic cycle. *Nature*, **419**, 224–232, doi:10.1038/nature01092.

Bayr, T., D. Dommenget, T. Martin, and S. Power, 2014: The eastward shift of the Walker circulation in response to global warming and its relationship to ENSO variability. *Climate Dyn.*, **43**, 2747–2763, doi:10.1007/s00382-014-2091-y.

Bonfils, C., and B. D. Santer, 2011: Investigating the possibility of a human component in various Pacific decadal oscillation indices. *Climate Dyn.*, **37**, 1457–1468, doi:10.1007/s00382-010-0920-1.

Cai, W., and Coauthors, 2014: Increasing frequency of extreme El Niño events due to greenhouse warming. *Nat. Climate Change*, **4**, 111–116, doi:10.1038/nclimate2100.

——, and Coauthors, 2015: Increased frequency of extreme La Niña events under greenhouse warming. *Nat. Climate Change*, **5**, 132–137, doi:10.1038/nclimate2492.

Capotondi, A., 2015: Atmospheric science: Extreme La Niña events to increase. *Nat. Climate Change*, **5**, 100–101, doi:10.1038/nclimate2509.

——, and M. Alexander, 2010: Relationship between precipitation in the Great Plains of the United States and global SSTs: Insights from the IPCC AR4 models. *J. Climate*, **23**, 2941–2958, doi:10.1175/2009JCLI3291.1.

——, Y.-G. Ham, A. Wittenberg, and J.-S. Kug, 2015a: Climate model biases and El Niño Southern Oscillation (ENSO) simulation. *U.S. CLIVAR Variations*, No. 13, U.S. CLIVAR Project Office, Washington, DC, 21–25.

——, and Coauthors, 2015b: Understanding ENSO diversity. *Bull. Amer. Meteor. Soc.*, **96**, 921–938, doi:10.1175/BAMS-D-13-00117.1.

Chung, C., S. Power, J. Arblaster, H. Rashid, and G. Roff, 2014: Nonlinear precipitation response to El Niño and global warming in the Indo-Pacific. *Climate Dyn.*, **42**, 1837–1856, doi:10.1007/s00382-013-1892-8.

Coats, S., J. E. Smerdon, B. I. Cook, and R. Seager, 2013: Stationarity of the tropical Pacific teleconnection to North America in CMIP5/PMIP3 model simulations. *Geophys. Res. Lett.*, **40**, 4927–4932, doi:10.1002/grl.50938.

Coelho, C., and L. Goddard, 2009: El Niño–induced tropical droughts in climate change projections. *J. Climate*, **22**, 6456–6476, doi:10.1175/2009JCLI3185.1.

Collins, M., and Coauthors, 2010: The impact of global warming on the tropical Pacific Ocean and El Niño. *Nat. Geosci.*, **3**, 391–397, doi:10.1038/ngeo868.

Compo, G., and P. Sardeshmukh, 2010: Removing ENSO-related variations from the climate record. *J. Climate*, **23**, 1957–1978, doi:10.1175/2009JCLI2735.1.

Dai, A., 2011: Characteristics and trends in various forms of the Palmer Drought Severity Index during 1900–2008. *J. Geophys. Res.*, **116**, D12115, doi:10.1029/2010JD015541.

——, and T. Wigley, 2000: Global patterns of ENSO-induced precipitation. *Geophys. Res. Lett.*, **27**, 1283–1286, doi:10.1029/1999GL011140.

——, K. Trenberth, and T. Qian, 2004: A global dataset of Palmer Drought Severity Index for 1870–2002: Relationship with soil moisture and effects of surface warming. *J. Hydrometeor.*, **5**, 1117–1130, doi:10.1175/JHM-386.1.

Guilyardi, E., and Coauthors, 2009: Understanding El Niño in ocean–atmosphere general circulation models—Progress and challenges. *Bull. Amer. Meteor. Soc.*, **90**, 325, doi:10.1175/2008BAMS2387.1.

Held, I., and B. Soden, 2006: Robust responses of the hydrological cycle to global warming. *J. Climate*, **19**, 5686–5699, doi:10.1175/JCLI3990.1.

Huang, P., S. Xie, K. Hu, G. Huang, and R. Huang, 2013: Patterns of the seasonal response of tropical rainfall to global warming. *Nat. Geosci.*, **6**, 357–361, doi:10.1038/ngeo1792.

Joseph, R., and S. Nigam, 2006: ENSO evolution and teleconnections in IPCC's twentieth-century climate simulations: Realistic representation? *J. Climate*, **19**, 4360–4377, doi:10.1175/JCLI3846.1.

Kao, H., and J. Yu, 2009: Contrasting eastern-Pacific and central-Pacific types of ENSO. *J. Climate*, **22**, 615–632, doi:10.1175/2008JCLI2309.1.

Karnauskas, K., R. Seager, A. Kaplan, Y. Kushnir, and M. Cane, 2009: Observed strengthening of the zonal sea surface temperature gradient across the equatorial Pacific Ocean. *J. Climate*, **22**, 4316–4321, doi:10.1175/2009JCLI2936.1.

Kug, J., S. An, Y. Ham, and I. Kang, 2010: Changes in El Niño and La Niña teleconnections over North Pacific–America in the global warming simulations. *Theor. Appl. Climatol.*, **100**, 275–282, doi:10.1007/s00704-009-0183-0.

Langenbrunner, B., and J. Neelin, 2013: Analyzing ENSO teleconnections in CMIP models as a measure of model fidelity in simulating precipitation. *J. Climate*, **26**, 4431–4446, doi:10.1175/JCLI-D-12-00542.1.

L'Heureux, M., S. Lee, and B. Lyon, 2013: Recent multidecadal strengthening of the Walker circulation across the tropical Pacific. *Nat. Climate Change*, **3**, 571–576, doi:10.1038/nclimate1840.

Lu, J., G. Chen, and D. Frierson, 2008: Response of the zonal mean atmospheric circulation to El Niño versus global warming. *J. Climate*, **21**, 5835–5851, doi:10.1175/2008JCLI2200.1.

Marvel, K., and C. Bonfils, 2013: Identifying external influences on global precipitation. *Proc. Natl. Acad. Sci. USA*, **110**, 19 301–19 306, doi:10.1073/pnas.1314382110.

Mears, C., B. Santer, F. Wentz, K. Taylor, and M. Wehner, 2007: Relationship between temperature and precipitable water changes over tropical oceans. *Geophys. Res. Lett.*, **34**, L24709, doi:10.1029/2007GL031936.

Meehl, G., and H. Teng, 2007: Multi-model changes in El Niño teleconnections over North America in a future

warmer climate. *Climate Dyn.*, **29**, 779–790, doi:10.1007/s00382-007-0268-3.

Peters, G., and Coauthors, 2013: The challenge to keep global warming below 2°C. *Nat. Climate Change*, **3**, 4–6, doi:10.1038/nclimate1783.

Power, S., F. Delage, C. Chung, G. Kociuba, and K. Keay, 2013: Robust twenty-first-century projections of El Niño and related precipitation variability. *Nature*, **502**, 541, doi:10.1038/nature12580.

Rayner, N., and Coauthors, 2006: Improved analyses of changes and uncertainties in sea surface temperature measured in situ since the mid-nineteenth century: The HadSST2 dataset. *J. Climate*, **19**, 446–469, doi:10.1175/JCLI3637.1.

Ruff, T., Y. Kushnir, and R. Seager, 2012: Comparing twentieth- and twenty-first-century patterns of interannual precipitation variability over the western United States and northern Mexico. *J. Hydrometeor.*, **13**, 366–378, doi:10.1175/JHM-D-10-05003.1.

Sandeep, S., F. Stordal, P. Sardeshmukh, and G. Compo, 2014: Pacific Walker circulation variability in coupled and uncoupled climate models. *Climate Dyn.*, **43**, 103–117, doi:10.1007/s00382-014-2135-3.

Santer, B. D., and Coauthors, 2009: Incorporating model quality information in climate change detection and attribution studies. *Proc. Natl. Acad. Sci. USA*, **106**, 14 778–14 783, doi:10.1073/pnas.0901736106.

Schubert, S., and Coauthors, 2009: A U.S. CLIVAR project to assess and compare the responses of global climate models to drought-related SST forcing patterns: Overview and results. *J. Climate*, **22**, 5251–5272, doi:10.1175/2009JCLI3060.1.

Seager, R., N. Naik, and L. Vogel, 2012: Does global warming cause intensified interannual hydroclimate variability? *J. Climate*, **25**, 3355–3372, doi:10.1175/JCLI-D-11-00363.1.

Seidel, D., Q. Fu, W. Randel, and T. Reichler, 2008: Widening of the tropical belt in a changing climate. *Nat. Geosci.*, **1**, 21–24, doi:10.1038/ngeo.2007.38.

Smith, T., R. Reynolds, T. Peterson, and J. Lawrimore, 2008: Improvements to NOAA's historical merged land–ocean surface temperature analysis (1880–2006). *J. Climate*, **21**, 2283–2296, doi:10.1175/2007JCLI2100.1.

Solomon, A., and M. Newman, 2012: Reconciling disparate twentieth-century Indo-Pacific ocean temperature trends in the instrumental record. *Nat. Climate Change*, **2**, 691–699, doi:10.1038/nclimate1591.

Sperber, K., and D. Kim, 2012: Simplified metrics for the identification of the Madden–Julian oscillation in models. *Atmos. Sci. Lett.*, **13**, 187–193, doi:10.1002/asl.378.

——, S. Gualdi, S. Legutke, and V. Gayler, 2005: The Madden–Julian oscillation in ECHAM4 coupled and uncoupled general circulation models. *Climate Dyn.*, **25**, 117–140, doi:10.1007/s00382-005-0026-3.

Stevenson, S., 2012: Significant changes to ENSO strength and impacts in the twenty-first century: Results from CMIP5. *Geophys. Res. Lett.*, **39**, L17703, doi:10.1029/2012GL052759.

——, B. Fox-Kemper, M. Jochum, R. Neale, C. Deser, and G. Meehl, 2012: Will there be a significant change to El Niño in the twenty-first century? *J. Climate*, **25**, 2129–2145, doi:10.1175/JCLI-D-11-00252.1.

Taylor, K., R. Stouffer, and G. Meehl, 2012: An overview of CMIP5 and the experiment design. *Bull. Amer. Meteor. Soc.*, **93**, 485–498, doi:10.1175/BAMS-D-11-00094.1.

Tokinaga, H., S.-P. Xie, C. Deser, Y. Kosaka, and Y. Okumura, 2012: Slowdown of the Walker circulation driven by tropical Indo-Pacific warming. *Nature*, **491**, 439–443, doi:10.1038/nature11576.

Trenberth, K., J. Fasullo, and L. Smith, 2005: Trends and variability in column-integrated atmospheric water vapor. *Climate Dyn.*, **24**, 741–758, doi:10.1007/s00382-005-0017-4.

Vecchi, G., and A. Wittenberg, 2010: El Niño and our future climate: Where do we stand? *Wiley Interdiscip. Rev.: Climate Change*, **1**, 260–270, doi:10.1002/wcc.33.

——, B. Soden, A. Wittenberg, I. Held, A. Leetmaa, and M. Harrison, 2006: Weakening of tropical Pacific atmospheric circulation due to anthropogenic forcing. *Nature*, **441**, 73–76, doi:10.1038/nature04744.

Watanabe, M., Y. Kamae, and M. Kimoto, 2014: Robust increase of the equatorial Pacific rainfall and its variability in a warmed climate. *Geophys. Res. Lett.*, **41**, 3227–3232, doi:10.1002/2014GL059692.

Wittenberg, A., 2015: Low-frequency variations of ENSO. *U.S. CLIVAR Variations*, No. 13, U.S. CLIVAR Project Office, Washington, DC, 26–31.

Xie, S., C. Deser, G. Vecchi, J. Ma, H. Teng, and A. Wittenberg, 2010: Global warming pattern formation: Sea surface temperature and rainfall. *J. Climate*, **23**, 966–986, doi:10.1175/2009JCLI3329.1.

Yeh, S., J. Kug, B. Dewitte, M. Kwon, B. Kirtman, and F. Jin, 2009: El Niño in a changing climate. *Nature*, **461**, 511–514, doi:10.1038/nature08316.

Zhou, Z., S. Xie, X. Zheng, Q. Liu, and H. Wang, 2014: Global warming–induced changes in El Niño teleconnections over the North Pacific and North America. *J. Climate*, **27**, 9050–9064, doi:10.1175/JCLI-D-14-00254.1.